Aligning and Testing the Ingot Wavefront Sensor in the Lab

Kalyan Kumar Radhakrishnan Santhakumari[a,b,†], Davide Greggio[a,b,†], Maria Bergomi[a,b,†], Simone Di Filippo[a,b,c], Valentina Viotto[a,b], Elisa Portaluri[d,b], Carmelo Arcidiacono[a,b], Marco Dima[a,b], Luigi Lessio[a,b], Luca Marafatto[a,b], Tommaso Furieri[e,f], Stefano Bonora[e], and Roberto Ragazzoni[a,b,c]

[a]INAF - Osservatorio Astronomico di Padova, Vicolo dell'Osservatorio 5, I-35122 Padova, Italy
[b]ADONI, Laboratorio Nazionale di Ottica Adattiva, Italy
[c]Dipartimento di Fisica e Astronomia, Università degli Studi di Padova, Vicolo dell'Osservatorio 3, I-35122 Padova, Italy
[d]INAF - Osservatorio Astronomico d'Abruzzo, Via Mentore Maggini, I-64100 Teramo, Italy
[e]CNR-IFN - Istituto di Fotonica e Nanotecnologie, via Trasea 7, 35131 Padova, Italy
[f]Department of Information Engineering, University of Padova, Via Gradenigo 6, 35131, Padova, Italy

ABSTRACT

The Sodium Laser Guide Star (Na-LGS) on the sky is not point-like, rather cigar-like when launched from the side of a large (or extremely large) telescope. The Na-LGS's 3D nature gave birth to the idea of a new pupil-plane wavefront sensor that can be deployed in a similar 3D manner - the Ingot Wavefront Sensor (I-WFS). The design of the I-WFS has developed over the last two years, and currently, the ingot prism has 3-faces, creating three pupils. Wavefront sensing can be done using these three pupils themselves as the signals or the slopes generated by the pupils.

At the INAF-Padova laboratory, we have realized a test-bench simulating the ELT* characteristics to test the I-WFS characteristics and an alignment procedure. We use simulations and lab data to compare, learn, and define a robust alignment procedure. Eventually, we expect to have an entirely automatized alignment procedure using the optical feedback from the I-WFS. In this article, we report the comparison between the laboratory data and the simulations representing (1) the sensitivity measurements of ingot prism misalignment for each degree of freedom with respect to its ideal, aligned position, and (2) the response of the I-WFS to known aberrations using a deformable lens. The final goal is the definition and description of the procedure to align the I-WFS.

Keywords: INGOT, wavefront sensing, Na-LGS, ELT, extended sources, laboratory test

1. INTRODUCTION

One of the common features of all the extremely large telescopes under construction is the Laser Guide Star (LGS) facility capable of creating artificial Sodium (Na) LGS for wavefront sensing.[1–3] The Na-LGS is created at an altitude ranging between $80 - 120$ km above the mean sea level. It is not a point source but extended in 3D. The cigar nature of the LGS is prominent when launched from the side of an extremely large telescope. The Na-LGS's 3D nature gave birth to the idea of a new pupil-plane wavefront sensor that can be deployed in a similar 3D manner - the Ingot Wavefront Sensor (I-WFS).[4]

The I-WFS can be considered an extension of the pyramid WFS for elongated objects.[5–7] Like in the pyramid WFS, the light of the source is split at the focal plane by a prism. Each beam exiting the prism is then re-imaged by an objective and forms an image of the telescope pupil. These pupils are used to calculate the wavefront slopes. However, in the case of LGSs, the image does not lie in a plane but rather in a 3D volume. If we

Send correspondence to KKRS. E-mail: kalyan.radhakrishnan@inaf.it, Telephone: +39 049 8293 447
† KKRS, DG, and MB contributed equally to the manuscript.
*By ELT, we mean European Extremely Large Telescope.

Adaptive Optics Systems VII, edited by Laura Schreiber, Dirk Schmidt, Elise Vernet, Proc. of SPIE
Vol. 11448, 1144860 · © 2020 SPIE · CCC code: 0277-786X/20/$21 · doi: 10.1117/12.2561075

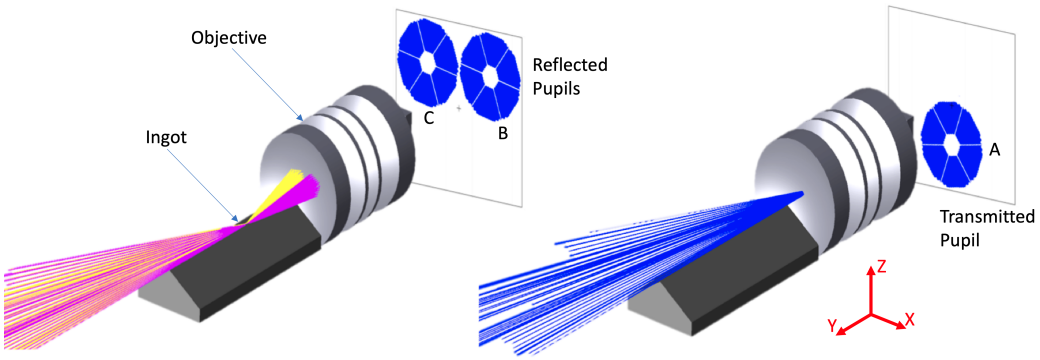

Figure 1. Schematic layout of the reflective ingot prism

approximate the LGS with a cylinder, the image of the axis of the cylinder made by the telescope is a segment, tilted by a certain angle with respect to the optical axis. Considering ELT characteristics and assuming an $F/5$ focal plane, it can be shown that the image of the axis of the cylinder is almost parallel to the optical axis and deviates from it by $\approx 5°$. Therefore, a prism placed with its long axis along the image will receive light at grazing incidence from the telescope. For this reason, to minimize light losses, the current design of the ingot prism foresees the use of a reflective prism rather than a refractive one.[8,9] The prism is a simple reflective roof whose edge is placed along the long axis of the LGS image to intercept only part of the LGS's light. The light reflected by the roof prism faces forms two images of the pupil, while the rest of the light reaches the re-imaging optics without touching the prism and forms a third image of the pupil.[10,11] We call the transmitted pupil as A and the reflected ones as B and C, as shown in Figure 1.

The advantage of this design (compared to the previous design, see this article[6] for details) is that it adapts to the variations in the thickness of the sodium layer (i.e., length of the LGS star) without changing the ingot prism. It is only necessary to have a roof prism long enough to accommodate the full length of the LGS image, even in the most elongated scenario. The ratio between the flux in the transmitted pupil and that in the reflected pupils can be adjusted moving the prism along the direction of the edge between the reflective faces. Like in a pyramid WFS, the pupils are used to calculate signals proportional to the first derivative of the wavefront. In the following equation, we define the signals S_x and S_y along the x and y directions (x denotes movements orthogonal to the elongation direction, while y denotes movements along the elongation direction) as:

$$\begin{aligned} S_x &= \frac{B-C}{A+B+C} - \frac{B_{ref}-C_{ref}}{A_{ref}+B_{ref}+C_{ref}}, \\ S_y &= \frac{A}{A+B+C} - \frac{A_{ref}}{A_{ref}+B_{ref}+C_{ref}}. \end{aligned} \tag{1}$$

The operation is done pixel-wise such that a signal S_x and S_y is obtained for every pixel. Note that we subtract the reference signal (also called reference slope), which is the signal that we consider the zero point of our calibration. This "zero" reference condition accounts for any misalignment (starting position of the ingot for the LGS image) and any static aberration present in the optical path.

2. LAB SETUP

The setup of the optical bench is composed of off-the-shelf components. It is specifically designed to simulate the imaging of an LGS source onto the ingot prism and to produce an image of the three pupils on a dedicated camera with proper sampling. The design reproduces as much as possible the ELT characteristics, such as:

1. the ratio between the distance of the Laser Launch Telescope from the optical axis and the entrance pupil diameter,
2. the physical size of the image on the ingot prism,

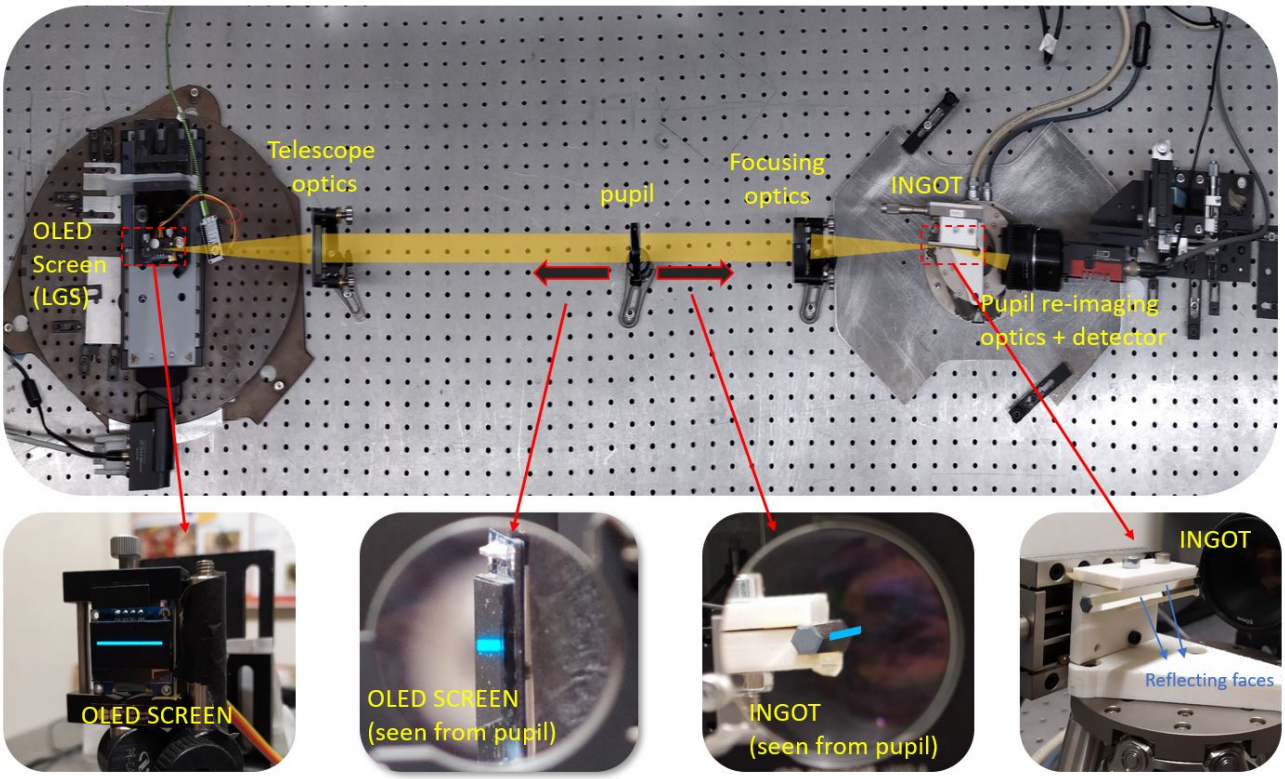

Figure 2. Top view of the optical bench setup used to test the ingot alignment procedure.

3. telecentric image space (on the ingot prism), and
4. the aspect ratio of the LGS (spot elongation to FWHM ratio).

The optical layout is based on a 1:1 re-imaging optical relay (see Figure 2). An achromatic doublet roughly collimates the light from the LGS source, and another one refocuses the light onto the ingot prism. A diaphragm, located between the lenses, acts as an aperture stop of the system and is placed such that the system is telecentric in image space. As pupil re-imaging optics, we use an $f = 50\ mm$ wide aperture photographic objective.

The source is an OLED screen programmable with an Arduino. The screen, an SSD1306 monochrome OLED display, has a format of 128x64 pixels with 170 μm pixel size. After testing other options such as laptop screens and an Apple iPad, we opted for an OLED screen, mainly to reduce the background noise of black pixels typical of other types of technologies. The tests presented in this paper use a uniform LGS intensity profile, however with the selected screen, it is easy to adjust the size and luminosity profile of the source by switching on and off individual pixels.

As the ingot prism, we use a hexagonal light pipe homogenizing rod whose external faces have been aluminized to obtain a reflective roof with an apex angle of 120°. This angle is the same one required at the ELT to achieve a proper separation of the reflected pupils. The ingot is mounted on an H-811 Hexapod from Physik Instrumente. The hexapod will allow precision movements in all six degrees of freedom of the ingot. Finally, the camera is a Prosilica GT3300 from Allied Vision. The detector is an 8 Megapixel CCD sensor with 5.5μm pixel size. With a 4x4 binning, the pupil diameter is sampled by $\approx 130\ px$.

3. SIMULATIONS

As a first step, we simulated the setup with the ray-tracing optical design software Zemax OpticStudio. The simulation allowed us to check the design parameters and get familiar with the I-WFS signals. To efficiently

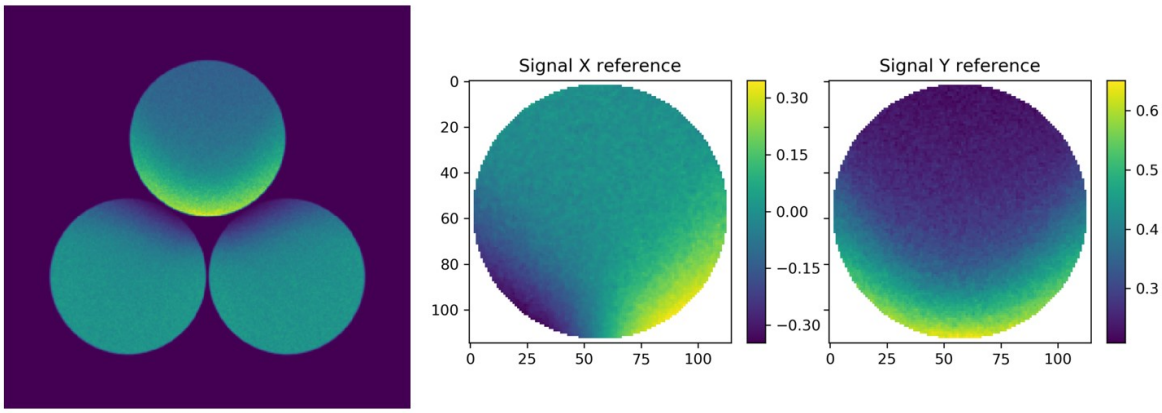

Figure 3. Left: Pupil illumination for the aligned condition. Right: Signals S_x and S_y are calculated from the pupils using the Equation (1).

simulate the source and get a good statistic in terms of rays/pixel in the image of the pupils, we developed a custom dynamic-link library source able to generate rays from a rectangular surface (or a cylindrical volume) and to aim them towards the entrance pupil of the system. The rays are traced through the system in a non-sequential fashion and recorded by a detector having $\approx 5\ px$ over the pupil diameter. The smaller sampling with respect to the real detector reduces the simulation time while keeping a reasonably low statistical noise. The source used in the simulations presented below is a rectangular source, 0.85 mm wide and 21.76 mm long, that approximately matches the average angular elongation expected on-sky and is compatible with the OLED screen's characteristics.

The pupil illumination pattern for the aligned condition is displayed in the left panel of Figure 3, where the transmitted pupil is at the top while the reflected pupils are at the bottom. In the central part of the image, the uneven illumination at the pupils' edges is a specific feature of the ingot and is due to its geometry. One may note the effect of uneven illumination in the signals (see right panel of Figure 3), which are not flat as in the case of a modulated pyramid wavefront sensor.

Note that diffraction effects are not accounted for in the simulations but are expected to be small due to the LGS's extended nature. Compared with the diffraction limited size of a 40-meter diameter telescope, in fact, the FWHM (short side) of the LGS is larger than $100\lambda/D$.

To calculate the signals, we developed a Python code to identify the pupils' position within an image autonomously. Individual pupils are extracted from the image and rotated/flipped to compensate for the effects induced by the reflection from the ingot. Once the pupils are co-aligned, they are used to calculate signals as indicated in equation (1).

The second step has been the simulation of I-WFS response to distortions (signals) by introducing in the Zemax model Zernike aberrations, expressed in terms of waves at 633 nm. Distortion has been added at the pupil level using a Biconic Zernike lens that allows to define the surface shape of the lens using Zernike Standard polynomials. The refractive index of the lens material has been set to 2 so that the transmitted wavefront error is exactly equal to the shape given to the lens's surface. For every aberration up to the fourth Zernike radial order, we simulated the resulting image of the pupils, and we compared the signals with those obtained in our lab setup (see following Section 4).

Finally, the last step has been to check the effects of misalignment of the ingot prism. We performed a sensitivity analysis by moving the ingot along each degree of freedom and looking at these observables: the distance between pupils, integrated flux within each pupil, and the variation produced on the signals S_x and S_y. In the aligned condition, the edge of the ingot is placed along the axis of symmetry (long direction) of the LGS image, the three pupils are equidistant one from the other, and both reflected pupils have the same integrated flux (see the right panel of Figure 3). The amount of light in the transmitted pupil is still a free parameter. For

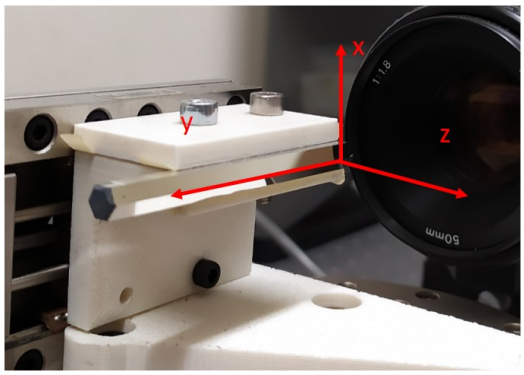

Figure 4. Coordinate system used in the simulations

the alignment procedure study, we set it approximately equal to the light of the reflected pupils, such as having $1/3^{rd}$ of the total flux in each pupil and maximizing the dynamic range available on the detector.

The reference coordinate system used for the analysis is represented in Figure 4. The origin is placed at the vertex of the ingot facing the camera; the Y-axis coincides with the edge between the reflective faces of the ingot and points towards the telescope, the X-axis points in the vertical direction with respect to the bench and aligned with the short side of the LGS image, the Z-axis is chosen to form a right-handed coordinate system. The pivot point for rotations is set at the origin of the coordinate system.

4. LABORATORY VALIDATION

We performed the lab validation of the simulated data of two key points:

1. the response of the I-WFS to known aberrations (described in Section 4.1),
2. the measurement sensitivity of the ingot prism to the misalignments from the ideal position (described in Section 4.2).

4.1 A deformable lens as an aberrator

In order to obtain actual I-WFS response to distortions (signals), we opted to insert in the optical path known aberrations and to compare them to the simulated ones. This allowed (1) to disentangle errors due to the setup itself, (2) to explore aspects which were not taken into account in the simulations, and (3) to speed up the understanding of the pros and cons of the new sensor and determine a path for the fine-tuning.

The means chosen to introduce the aberrations is a Multi-Actuator Lens (MAL), presenting two notable advantages with respect to other solutions: (1) the MAL does not require to modify the existent optical path and (2) its installation is extremely straightforward, common off-the-shelf lab parts can be used to hold it, its electronics is very compact, and the lens is operated through a standard laptop.

4.1.1 Multi-actuator lens

The Multi-Actuator Lens, developed at the CNR laboratories in Padova, is a piezoelectric-type wavefront corrector composed of two thin glass membranes, spaced apart by a chamber filled with transparent oil. Its transmission (in the absence of anti-reflection coatings) is about 90% in the range $400 - 1100\ nm$. Each glass membrane is bonded to a piezoelectric ring divided into 9 sectors on each side, representing the actuators. By applying a driving voltage (maximum range $+/-125\ V$) to each sector, it is possible to bend the glass membrane locally. Linearly combining the actuators, it is possible to generate aberrations up to the 4th radial order of Zernike polynomials, with a maximum amplitude (mode dependent) of up to a dozen sodium wavelengths. In the astronomical field, MAL has proven its potential both during on-sky observations for small telescopes[12] and in a laboratory experiment to compensate low order Non Common Path Aberrations (NCPA), to exploit the full capabilities of a pyramid wavefront sensor.[13] Further details on the MAL (transmission spectrum, response time curve, chromaticity, etc.) can be found in citations here.[14–16]

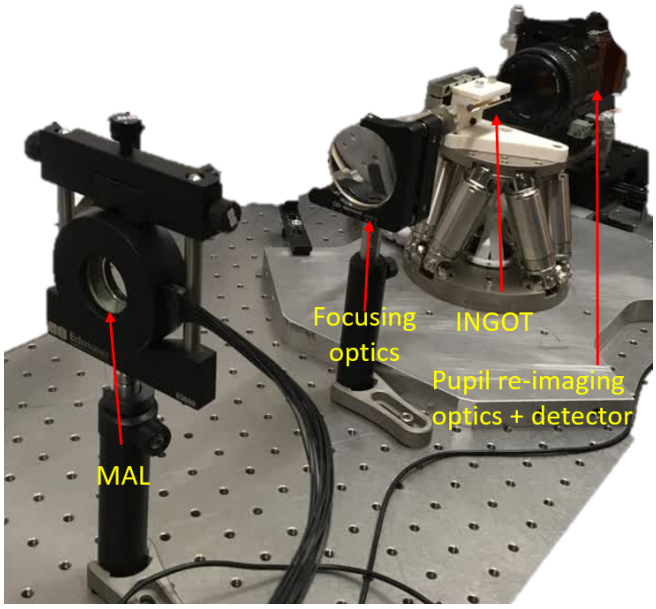

Figure 5. MAL inserted at the pupil location in the I-WFS test-bench, in order to introduce known aberrations.

Table 1. MAL maximum applicable aberration per Zernike mode (in waves rms, $\lambda = 633\ nm$)

Aberration type	**Maximum Aberration amplitude (waves rms)**
Tip/Tilt	4.3/4.4
Defocus	3
Astigmatism (x/y)	2.3/2.4
Coma (x/y)	0.65/0.6
Trefoil (x/y)	1.3/2
Spherical	0.55
Secondary astigmatism (x/y)	0.33/0.35
Tetrafoil (x/y)	0.65/0.55

4.1.2 Experimental setup

For this experiment, we placed a MAL with a 25 mm clear aperture and 18 actuators (9 on each side of the lens) at the pupil of the setup described in Section 2 (see Figure 5). It has to be noted that all tests involving the MAL were performed with an Apple iPad screen (9.7" back-illuminated LED, 2048x1536 pixels, 264 ppi) as an LGS source. Also, the source's size was different from the one used on the OLED screen and was 44.5 mm in length and 1 mm in width. The MAL had been previously characterized and some tests were performed to determine how accurately the aberrations could be reproduced, finding a repeatability within 0.1λ rms.

After aligning the I-WFS to the source, we collected data for two tests: (1) I-WFS signal response to input aberration and (2) I-WFS signal correlation with the amplitude of the input aberration. For the first test, for each Zernike mode, we applied the highest possible achievable amplitude (see Table 1), which, as stated earlier, is mode dependent. After applying each aberration, we saved 10 frames (an example, trefoil, is shown in the right panel of Figure 6). We also collected 10 frames with the MAL flat, acting as an optical window, for static signal subtraction (see left panel of Figure 6). For the second test, we applied Trefoil x aberration to the MAL, each time varying its amplitude between +2 and -1 (λ rms).

4.1.3 Results and Analysis

We estimated the signals from the three pupils as described in Section 3. When analyzing them and comparing to the simulations, a few fine-tuning of parameters, such as clocking the simulated signals to match the setup orientation, were required. Figure 7 shows a few examples (defocus, astigmatism, trefoil) of the signals simulated

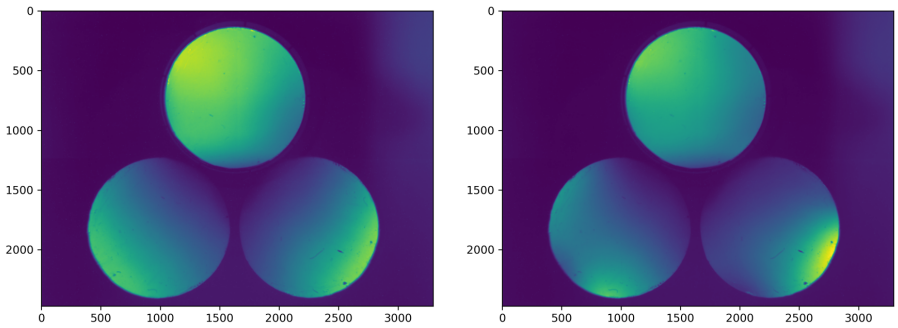

Figure 6. Left: I-WFS pupil when the MAL is flat, Right: I-WFS pupil when trefoil is applied on the MAL.

(top row) and the ones obtained on the lab setup introduced by the MAL (bottom row). The signals extracted from real images appear qualitatively similar to the simulated ones. However, the intensity differs between simulated and real data. The real data shows higher signal X and lower signal Y in comparison to the simulated one. The main problem was identified in the source itself, particularly the background generated by black pixels, which produced a lot of flux in the transmitted pupil, thus reducing the system's dynamical range. Moreover, the illumination of the pupil was not uniform due to the angular emissivity profile of the screen, which can be seen as a gradient in the sum of the three pupils, see Figure 8.

Given the above considerations, in order to reduce the impact of the source-related issues, to determine the correlation of I-WFS responses to variation of aberration amplitude, we considered the response of a few sub-apertures located in areas more strongly affected by Trefoil aberration, as depicted in Figure 9. There is a clear linear relation between the applied input aberration and the retrieved signal for the two sub-aperture cases. However, it can be noticed that the signal Y is always lower than signal X. For this reason, we have decided to opt for a different source with a lower background noise, the OLED source, used for the other experiments described in this paper.

New tests to determine I-WFS response to aberrations introduced with the MAL were postponed to a more mature phase of the experiment, in order to focus on the automatization of the alignment procedure.

4.2 Sensitivity measurements of the misalignments

The effect produced by each degree of freedom on inter-pupil distance and flux was first simulated with Zemax and then verified with the lab setup by using the hexapod to precisely move the ingot prism. Table 2 reports a summary of the observables produced by each degree of freedom. The rotation affects mainly the position of pupils, while decenter affects only the flux. In the table, we distinguish between reflected and transmitted pupils and give an idea of the magnitude of the change by using ++ for stronger variations and + for weaker variations. Note that decenter Y has a weaker effect with respect to other degrees of freedom because it corresponds to the direction of elongation, which, as expected, reduces the sensitivity to aberrations and movements in general.

Table 2. Degrees of freedom and corresponding observables

Degree of Freedom	**Transmitted Flux**	**Reflected Flux**	**Distance between Transmitted & Reflected Pupils**	**Distance between the Reflected Pupils**
Decenter X	+	++		
Decenter Y	+	+		
Decenter Z	++	++		
Tilt around X			++	++
Tilt around Y			++	
Tilt around Z		++	++	+

Figures 10 & 11 report the signals produced by each degree of freedom from the Zemax simulations and the laboratory verification, respectively. The comparison is only qualitative because the simulated amplitudes are

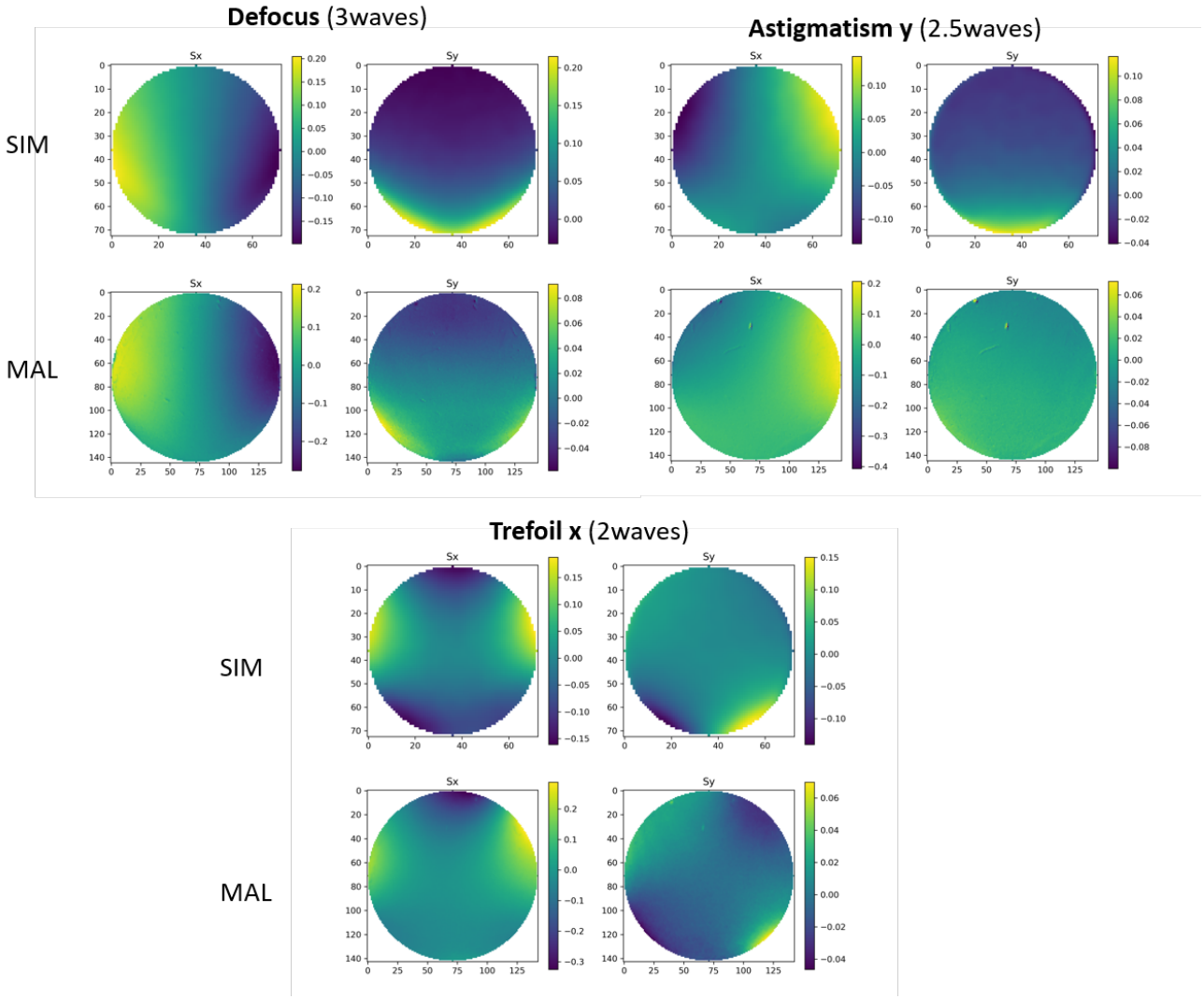

Figure 7. Simulated (top row) vs lab (bottom row) signals for three aberrations: defocus, astigmatism and trefoil. The amplitude of the aberrations are 3, 2.5 and 2 waves rms, respectively (the maximum achievable by this MAL, as per Table 1). Please note that colour bars are different.

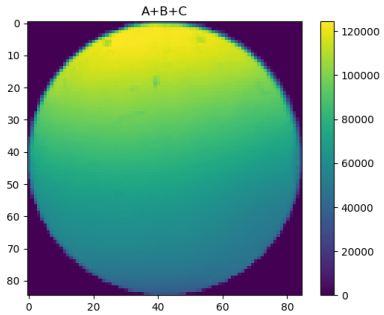

Figure 8. Pupil obtained from the sum of the three pupils in the case where no aberrations where introduced in the setup. A clear gradient along the Y axis is visible.

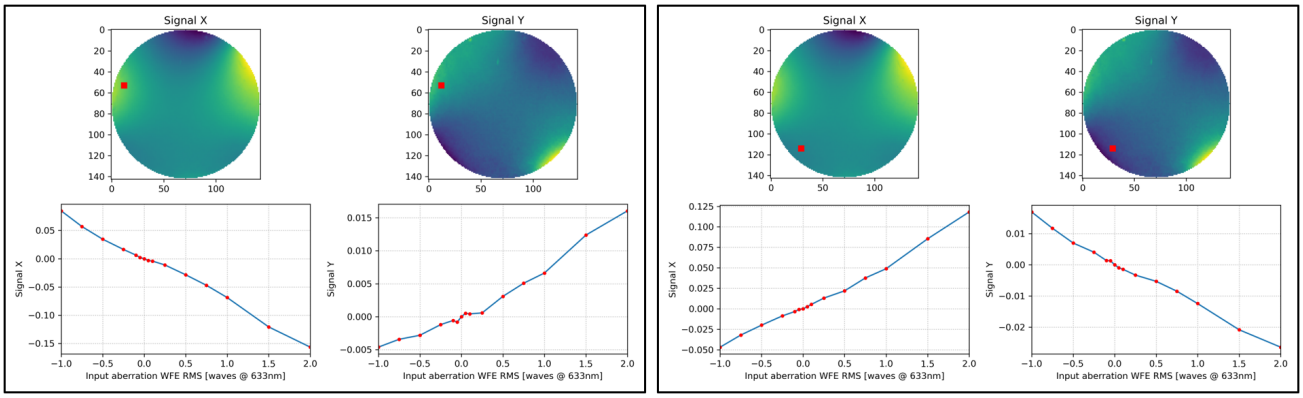

Figure 9. Trefoil signals computed for two sub-apertures (left and right panels). Top panel shows the trefoil signals and the identified sub-aperture for the analysis. Lower panel plots the I-WFS signals for each applied aberration amplitude (*red dots*).

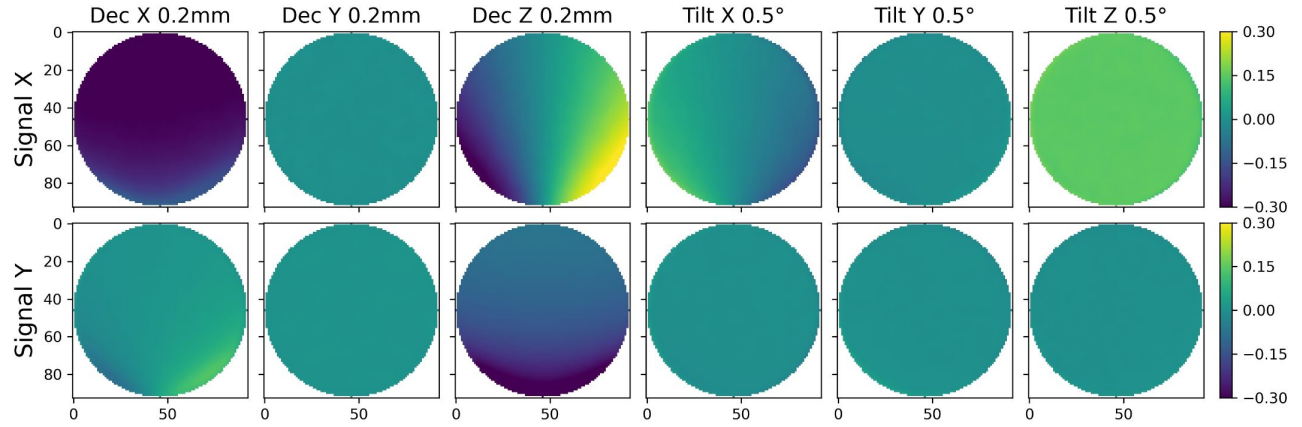

Figure 10. Variation of signal produced by each degree of freedom. Results from simulations.

different from the lab measurements, but the signals produced by the simulations and lab verification match quite well. Note that tilt around the Y-axis produces a minimal signal. Indeed, this degree of freedom has little relevance for the ingot alignment to the LGS source. In fact, the 3D image of an LGS has, to a good approximation, a cylindrical symmetry, and rotation around the Y-axis does not impact the alignment. The signal is negligible also in the case of a rectangular source like the one used in our simulations and lab setup. The only effect expected by tilt Y is a change of the average angle of incidence on the reflective faces of the ingot, which can have an impact on the average reflectivity. In practice, since the main observable produced is a rotation of the reflected pupils, we use this degree of freedom only during the first alignment to have the reflected pupils aligned horizontally on the detector. Then, we do not consider it anymore. Note that, due to the source's elongation, the signal produced by decenter Y is weaker than the others.

5. ALIGNMENT PROCEDURE

Given the results of the sensitivity analysis, the procedure developed for the first alignment of the ingot consists of the following steps:

1. Move tilt Y and tilt Z to achieve the same distance between transmitted and reflected pupils and to have the reflected pupils aligned horizontally on the detector.
2. Move tilt X to have a separation of a few pixels between the pupils.
3. Move decenter X to equalize the flux in the reflected pupils.

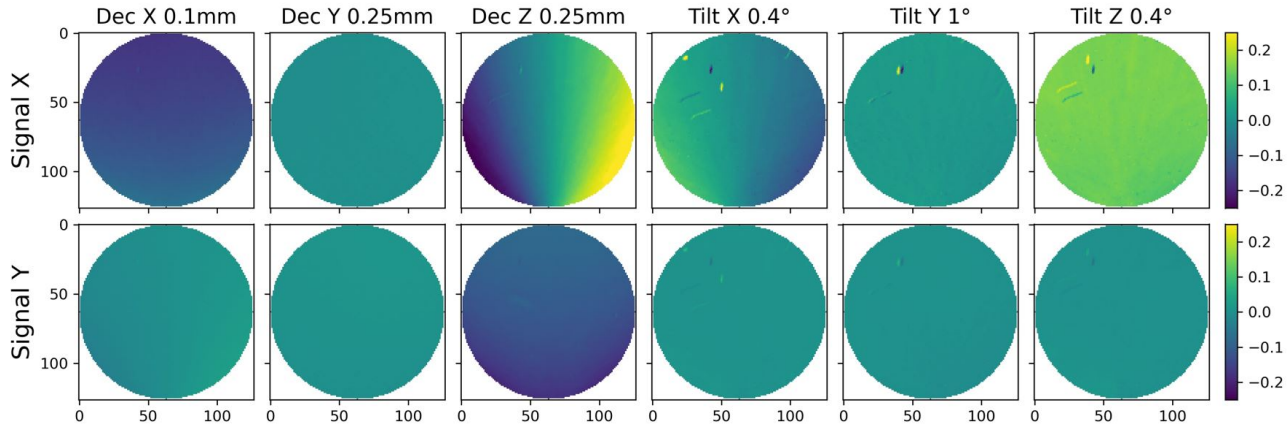

Figure 11. Variation of signal produced by each degree of freedom. Results from lab measurements.

4. Move decenter Z to achieve a flat signal x in the top part of the pupil (in the bottom part of the pupil, the signal is not flat as shown in Figure 3).

5. Move decenter Y to have the same flux in all the 3 pupils.

The procedure above should be iterated a few times because the observables are not completely independent one from the other. At the end of this procedure, the ingot is aligned with the proper angles with respect to the telescope optical axis so that the pupils are properly separated, and the flux within each pupil corresponds to the desired one. If now we consider a movement of the LGS on sky, this reflects in a movement of its image on the ingot. This will produce a variation of the flux and signals, but will not change the position of the pupils because that depends solely on the relative alignment between the ingot and the telescope. Thus, the distance between pupils cannot be used to keep the LGS image aligned to the ingot during operation and we can only rely on the measurement of signals.

5.1 Interaction matrix of misalignments

The strategy adopted to reconstruct misalignments between the ingot and the LGS image is based on an interaction matrix calculation. For each degree of freedom, we calculate the variation of the signal produced. We use a modal reconstruction approach by fitting the signals S_x and S_y with low order Zernike polynomials to mitigate the effects of noise and higher-order aberrations that are not related to misalignment. The fitted Zernike polynomials' coefficients are then used to build the reconstruction matrix needed to calculate the actual misalignment between the ingot and LGS image. The reconstructed misalignments are then corrected in a closed-loop fashion.

The procedure described above has been tested directly on the optical bench. After performing the first alignment of the ingot to the LGS image, we moved the hexapod along each degree of freedom (except tilt around Y) recording the signals necessary to calculate the interaction matrix. Then, we calculated the reconstruction matrix by taking the pseudo-inverse of the interaction matrix. We thus obtained what we call a "laboratory reconstruction matrix". We applied the same procedure on simulated images as well, obtaining a "synthetic reconstruction matrix". The rationale of building a synthetic reconstruction matrix is that of testing the consistency between the model and the real setup. Moreover, if we can rely on a synthetic reconstruction matrix, the alignment procedure would not necessarily require a dedicated calibration source inside the instrument.

5.2 Testing the misalignment reconstruction matrices

The reconstruction matrices have been tested by adding a random combination of misalignments to the ingot using the hexapod and reconstructing it from the recorded signals. We performed multiple iterations in a closed-loop fashion and the system converges back to the aligned condition. Figure 12 shows the residual misalignment error as a function of the iteration number for one of the tested cases. The left panel plot represents the laboratory

reconstruction matrix, while that on the right represents the synthetic reconstruction matrix, starting from the same misaligned condition. In both cases, the ingot converges back to the aligned condition, but with slightly larger residuals in the case of the synthetic IM. This is somewhat expected because the simulations do not exactly match the real setup. Despite this, the residuals are $< 10\%$ with respect to the input misalignment, and the loop is stable.

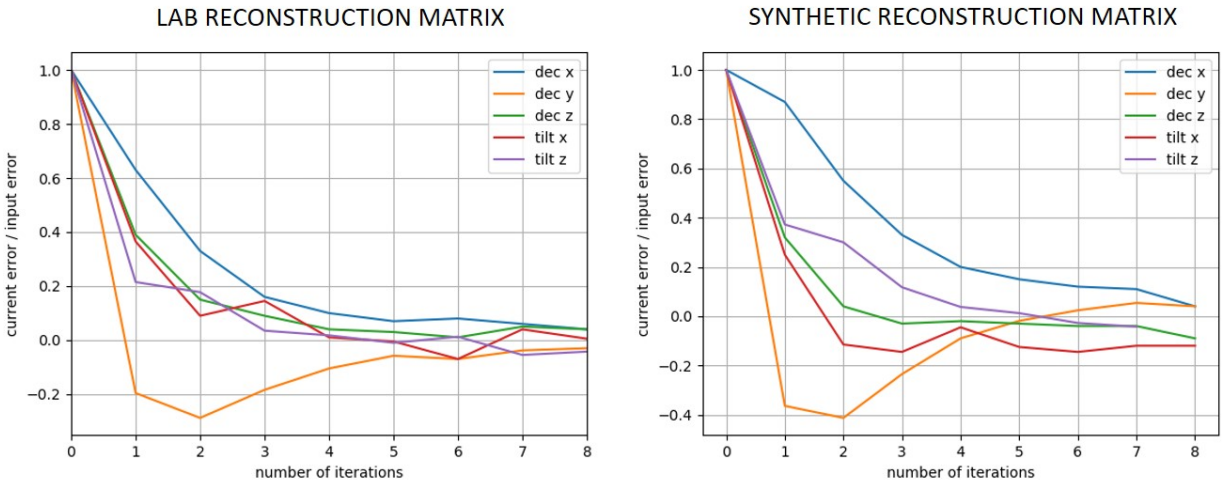

Figure 12. Residual alignment error normalized by the input error as a function of the iteration number for the laboratory IM (left) and the synthetic IM (right).

The next step consists of fully automatizing the alignment loop to speed up the tests and perform a statistical analysis of the convergence. This will be done by remotely controlling the hexapod and the camera and developing Python scripts to automatize the calculation of signals, the reconstruction, and the compensation processes. An automatized procedure will allow us to perform faster analyses and avoid errors and demonstrate that the same procedure can be used during operation at the telescope to maintain the alignment between ingot and LGS.

6. CONCLUSION & FUTURE STEPS

We have an optical setup mimicking the ELT characteristics at the INAF-Observatory of Padova to test the I-WFS and its alignment procedure. Aligning the ingot prism to the LGS source, with its 6 degrees of freedom is not an easy task and requires several simulations and tests. We have now devised an alignment procedure and tested its working and efficacy, as described in the paper. We are currently in the process of fully automatizing the alignment procedure. Afterward, we will retest the performance of the I-WFS using, as a first step, static aberration, followed by closed-loop operations by applying dynamic disturbances. The setup will evolve in time to accommodate a deformable mirror and eventually a pyramid WFS and/or a Shack-Hartmann WFS to compare the performances. We also plan to introduce the source profile taking into account temporal and spatial variability to mimic as much as possible the real scenario. Our final goal is to reach a stage to use the laboratory setup to compare I-WFS performance using the lab data with the end-to-end simulations.[17]

ACKNOWLEDGMENTS

Funding to support the laboratory activities described in this paper came from the INAF Progetto Premiale "Ottica Adattiva Made in Italy per i grandi telescopi del futuro".

REFERENCES

[1] Boyer, C., Ellerbroek, B., Gilles, L., and Wang, L., "The TMT Laser Guide Star Facility," in [*Adaptative Optics for Extremely Large Telescopes*], 04004 (Jan. 2010).

[2] D'Orgeville, C., Bouchez, A., Conan, R., Espeland, B., Gardhouse, R., Hart, J., Price, I., Trancho, G., and Uhlendorf, K., "GMT Laser Guide Star Facility," in [*Proceedings of the Third AO4ELT Conference*], Esposito, S. and Fini, L., eds., 14 (Dec. 2013).

[3] Bonaccini Calia, D., Guidolin, I., Friedenauer, A., Hager, M., Karpov, V., Pfrommer, T., Holzlöhner, R., Lewis, S., Hackenberg, W., Lombardi, G., Centrone, M., and Pedichini, F., "The ESO transportable LGS Unit for measurements of the LGS photon return and other experiments," in [*Modern Technologies in Space- and Ground-based Telescopes and Instrumentation II*], Navarro, R., Cunningham, C. R., and Prieto, E., eds., *Society of Photo-Optical Instrumentation Engineers (SPIE) Conference Series* **8450**, 84501R (Sept. 2012).

[4] Ragazzoni, R., Portaluri, E., Viotto, V., Dima, M., Bergomi, M., Biondi, F., Farinato, J., Carolo, E., Chinellato, S., Greggio, D., Gullieuszik, M., Magrin, D., Marafatto, L., and Vassallo, D., "Ingot Laser Guide Stars Wavefront Sensing," *AO4ELT5 Proceedings* (Aug. 2017).

[5] Ragazzoni, R., Greggio, D., Viotto, V., Di Filippo, S., Dima, M., Farinato, J., Bergomi, M., Portaluri, E., Magrin, D., Marafatto, L., Biondi, F., Carolo, E., Chinellato, S., Umbriaco, G., and Vassallo, D., "Extending the pyramid WFS to LGSs: the INGOT WFS," in [*Adaptive Optics Systems VI*], Close, L. M., Schreiber, L., and Schmidt, D., eds., *Society of Photo-Optical Instrumentation Engineers (SPIE) Conference Series* **10703**, 107033Y (July 2018).

[6] Viotto, V., Portaluri, E., Arcidiacono, C., Ragazzoni, R., Bergomi, M., Di Filippo, S., Dima, M., Farinato, J., Greggio, D., Magrin, D., and Marafatto, L., "Dealing with the cigar: preliminary performance estimation of an INGOT WFS," in [*Adaptive Optics Systems VI*], Close, L. M., Schreiber, L., and Schmidt, D., eds., *Society of Photo-Optical Instrumentation Engineers (SPIE) Conference Series* **10703**, 107030V (July 2018).

[7] Ragazzoni, R., Viotto, V., Portaluri, E., Bergomi, M., Greggio, D., Di Filippo, S., Radhakrishnan, K., Umbriaco, G., Dima, M., Magrin, D., Farinato, J., Marafatto, L., Arcidiacono, C., and Biondi, F., "Pupil plane wavefront sensing for extended and 3d sources," in [*AO4ELT6*], (2019).

[8] Di Filippo, S., Greggio, D., Bergomi, M., Radhakrishnan, K., Portaluri, E., Viotto, V., Arcidiacono, C., Magrin, D., Marafatto, L., Dima, M., Ragazzoni, R., Janin-Portirond, P., Schatz, L., Neichel, B., Fauvarque, O., and Fusco, T., "Ingot wavefront sensor: from the optical design to a preliminary laboratory test," in [*AO4ELT6*], (2019).

[9] Arcidiacono, C., Di Filippo, S., Santhakumari, K. K. R., Greggio, D., Viotto, V., Portaluri, E., Ragazzoni, R., Bergomi, M., Marafatto, L., Dima, M., Magrin, D., Janin-Potiron, P., Fusco, T., Neichel, B., and Fauvarque, O., "Fourier optics Ingot WFS End2End numerical simulations," in [*This Conference*], *Society of Photo-Optical Instrumentation Engineers (SPIE) Conference Series* (Dec. 2020).

[10] Viotto, V., Portaluri, E., Arcidiacono, C., Bergomi, M., Di Filippo, S., Greggio, D., Radhakrishnan, K., Dima, M., Farinato, J., Magrin, D., Marafatto, L., and Ragazzoni, R., "Ingot wavefront sensor: Simulation of pupil images," in [*AO4ELT6*], (2019).

[11] Portaluri, E., Viotto, V., Ragazzoni, R., Arcidiacono, C., Bergomi, M., Greggio, D., Radhakrishnan, K., Di Filippo, S., Marafatto, L., Dima, M., Biondi, F., Farinato, J., and Magrin, D., "Ingot wfs for lgss: First results from simulations," in [*AO4ELT6*], (2019).

[12] Quintavalla, M., Spagnol, M., Abe, L., Carbillet, M., Aristidi, E., Mocci, J., Muradore, R., and Bonora, S., "XSAO: an extremely small adaptive optics module for small-aperture telescopes with multiactuator adaptive lens," *Journal of Astronomical Telescopes, Instruments, and Systems* **6**, 029004 (Apr. 2020).

[13] Quintavalla, M., Bergomi, M., Magrin, D., Bonora, S., and Ragazzoni, R., "Correction of non-common path aberrations in pyramid wavefront sensors to recover the optimal magnitude gain using a deformable lens," *Appl. Opt.* **59**, 5151–5157 (Jun 2020).

[14] Moosavi, S. A., Quintavalla, M., Mocci, J., Muradore, R., Saghafifar, H., and Bonora, S., "Improvement of coupling efficiency in free-space optical communication with a multi-actuator adaptive lens," *Opt. Lett.* **44**, 606–609 (Feb 2019).

[15] Negro, M., Quintavalla, M., Mocci, J., Ciriolo, A. G., Devetta, M., Muradore, R., Stagira, S., Vozzi, C., and Bonora, S., "Fast stabilization of a high-energy ultrafast OPA with adaptive lenses," *Scientific Reports* **8**, 14317 (Sept. 2018).

[16] Bonora, S., Jian, Y., Zhang, P., Zam, A., Pugh, E. N., Zawadzki, R. J., and Sarunic, M. V., "Wavefront correction and high-resolution in vivo oct imaging with an objective integrated multi-actuator adaptive lens," *Opt. Express* **23**, 21931–21941 (Aug 2015).

[17] Portaluri, E., Viotto, V., Ragazzoni, R., Arcidiacono, C., Santhakumari, K. K. R., Bergomi, M., Greggio, D., Di Filippo, S., Farinato, J., and Magrin, D., "Evaluating the performance of an Ingot wavefront sensor for the ELT: good news from simulations," in [*This Conference*], *Society of Photo-Optical Instrumentation Engineers (SPIE) Conference Series* (Dec. 2020).